Ionics (2020) 26:75–83
https://doi.org/10.1007/s11581-019-03220-0

ORIGINAL PAPER

Facile synthesis of $Ag/ZnMn_2O_4$ hybrids as improved anode materials for lithium-ion batteries

Chao He[1] · Xiao-Bin Zhong[2] · Xiao-Xiao Wang[2] · Jia-Hui Chen[1] · Fan Gao[2] · Qing-Chi Xu[1] · Zhong-Qun Tian[2] · Jian-Feng Li[1,2,3]

Received: 22 June 2019 / Revised: 13 August 2019 / Accepted: 16 August 2019 / Published online: 24 August 2019

Abstract

With the constantly increasing demands of high energy density and long life span energy storage devices, people are looking for high-performance and safe anode materials as alternatives to replace graphite in lithium-ion batteries. A facile coprecipitation method has been developed to synthesize $Ag/ZnMn_2O_4$ (Ag/ZMO) hybrids with various weight ratios of Ag as anode materials in lithium-ion batteries. Electrochemical measurements indicate that the addition of Ag nanoparticles not only improves the conductivity of electrode material but also enhances the initial coulombic efficiency and the cycle stability of electrode materials. After 100 cycles at 100 mA g^{-1}, the optimum Ag/ZMO hybrid can still maintain an ultra-high average capacity of 1300 mAh g^{-1}. It is anticipated that our work may open up a new avenue to rapidly and massively produce various anode materials decorated with Ag nanoparticles for lithium-ion batteries.

Keywords Ag nanoparticles · $ZnMn_2O_4$ · Lithium-ion batteries · Enhanced cycling performance

Introduction

With the rapid development of society, the growing energy markets urgently require lithium-ion batteries with higher energy density [1–3]. However, the commercial graphite anode materials are far from the market demands because of the low theoretical specific capacity (372 mAh g^{-1}) [4–6]. Therefore, seeking for high-performance, low-cost, and easy-to-prepare anode materials for lithium-ion batteries have become a popular research area for researchers [2, 7–10]. As novel anode materials, bimetallic oxides with high theoretical capacity were widely studied in the past decades [11–19]. Bimetallic oxides often undergo several chemical reactions during charge and discharge processes [20–22]. Due to the nature of metal, these reactions occur at different potentials, which can suppress the volume changes of the electrode material during reactions in some degree [22, 23]. As a common bimetallic oxide, $ZnMn_2O_4$ (ZMO) not only possesses the above advantages but also has a lower discharge voltage platform, and thus results in a higher output voltage, which drive researchers to study it extensively [13, 14, 24–32]. Yan's group [31] obtained a high-performance mesoporous ZMO microtubule via a biomorphic strategy. The ZMO mesoporous microtubules exhibited larger surface area and faster reaction kinetics, which led to high capacity, rate capacity, and cycling stability in both lithium-ion and sodium-ion batteries. Zhang et al. [33] designed a 2D-on-3D structured $ZnMn_2O_4$@CMK-3 hybrid through a common hydrothermal method. Benefiting from its unique nanostructure, the $ZnMn_2O_4$@CMK-3 hybrid exhibited a superior lithium storage performance.

However, the volume changes of the bimetallic oxide during the charge and discharge processes are still inevitable [34]. After long-term cycles, electrode materials will pulverize and fall off from the current collector, resulting in fatal capacity degradation [35]. Moreover, the poor conductivity of bimetallic oxide hinders

Electronic supplementary material The online version of this article (https://doi.org/10.1007/s11581-019-03220-0) contains supplementary material, which is available to authorized users.

✉ Qing-Chi Xu
xuqingchi@xmu.edu.cn

✉ Jian-Feng Li
Li@xmu.edu.cn

[1] Department of Physics, Xiamen University, Xiamen 361005, China

[2] MOE Key Laboratory of Spectrochemical Analysis and Instrumentation, State Key Laboratory of Physical Chemistry of Solid Surfaces, iChEM, College of Chemistry and Chemical Engineering, Xiamen University, Xiamen 361005, China

[3] Shenzhen Research Institute of Xiamen University, Shenzhen 518000, China

the ion diffusion and transfer during charge/discharge process. To overcome the above inherent drawbacks, the modifications of bimetallic oxides electrode materials are mainly focused on nanosization and carbon coating. Shen's group [36] synthesized a unique hierarchical 3D $ZnCo_2O_4$ nanowire with high capacity, excellent cycling performance, and good rate capability. Lu et al. [37] prepared a thin carbon layer coated $ZnSn_2O_4$ mesoporous nanocube for LIBs and also achieved an excellent cycling performance. Furthermore, Jiang et al. [38] reported that the Ag/mesoporous carbon nanotube hybrids showed a better cycling performance than that of mesoporous carbon nanotube. Both experimental results and theoretical calculations indicated that the presence of Ag nanoparticles on mesoporous carbon nanotubes could inhibit the continuous generation of solid electrolyte interphase (SEI) film, which led to high initial coulombic efficiency (CE) and enhanced cycling performance. Inspired by this and enlightened by the intrinsic merits of ZMO, it is thus highly desirable to judiciously integrate Ag nanoparticles with ZMO in a close integration manner which would take full advantage of the synergistic interaction between them giving rise to promising electrochemical performances. However, to the best of our knowledge, the addition of Ag nanoparticles in ZMO to improve the electrochemical performances and cycle stability of ZMO as anode material in lithium ion battery has not been reported yet.

Herein, a simple and rapid coprecipitation method has been designed to synthesize $ZnMn_2O_4$–Ag (ZMO–Ag) hybrids with various weight ratios of Ag as anode materials for lithium ion battery. Ag/ZMO hybrids can be rapidly prepared with a relatively low cost and more likely to be applied in industrial production. The decoration of Ag nanoparticles not only can improve the conductivity of ZMO but also can effectively inhibit the continuous generation of SEI film, which definitely will benefit for the improvement of the initial CE. The electrochemical measurements verify that the optimum Ag/ZMO hybrid (ZMO–Ag–2) demonstrates higher reversible capacity and better cycling stability compared with that of pure ZMO. After 100 cycles at 100 mA g^{-1}, the ZMO–Ag–2 still exhibits an ultra-high reversible capacity of 1300 mAh g^{-1}, which proves that ZMO–Ag–2 probably can be considered a promising anode material for lithium-ion batteries in the future. Furthermore, this modification method provides a new idea for the follow-up design and modification of electrode materials.

Experimental

All of the reagents used in this article are analytical grade and used without further purification.

Synthesis of ZMO

Firstly, according to the mole ratio of the element, a certain amount of $Zn(NO_3)_2 \times 6H_2O$ and $Mn(NO_3)_2$ were dissolved in 100 mL water and labeled as solution A. Another 100 mL saturated oxalate ethanol solution was prepared and labeled as solution B. Then, solution A was injected into solution B at a rate of 5 mL min^{-1} under continuous stirring. Subsequently, the precipitation was centrifuged, washed with DI water 3 times, and dried in the oven at 100 °C. ZMO was obtained after being calcined in tube furnace at 550 °C for 2 h.

Synthesis of ZMO–Ag

Briefly, an appropriate amount of $AgNO_3$ was dissolved in solution A. Then, the rest of the process was similar to the preparation of ZMO. According to the theoretical weight ratio of Ag:ZMO = 0.5%, 1%, 3%, the obtained Ag/ZMO hybrids were labeled as ZMO–Ag–1, ZMO–Ag–2, ZMO–Ag–3, respectively.

Material characterizations

The crystal structure and bonding information of the as-prepared materials were characterized by XRD (Rigaku Ultima IV; Cu Kα radiation, 1.5406 Å) and Xplora plus, respectively. FESEM (Hitachi S–4800) was used to characterize the morphology features and EDS analysis was carried out in the SEM to determine the approximate element ratio. In addition, HRTEM (Tecnai, F30) was applied to characterize the crystal structure. XPS measurements were carried out on the XPS apparatus (PHI QUANTUM 2000) and all binding energies were referred to the C 1 s peak of 284.8 eV as an internal standard.

Preparation of electrodes and electrochemical characterization

Typically, 70 wt% as-prepared Ag/ZMO hybrids, 20 wt% acetylene black, and 10 wt% sodium carboxymethylcellulose were mixed into homogeneous slurry. Then, the black slurry was coated with copper foil collectors and dried at 120 °C under vacuum overnight to obtain anode electrodes. All of the electrochemical properties were tested with typical CR2032 coin half-cells. Metal lithium foil was used as the counter electrode, cellgard 2400 was used as the separator, and 1 M $LiPF_6$ dissolved in ethylmethyl carbonate, ethylene carbonate, and diethyl carbonate (1:1:1 v/v/v) served as the electrolyte. The galvanostatic charge–discharge test was performed on LAND2001 with a voltage range of 0.01–3.0 V. The cyclic voltammetry (CV) was measured with electrochemical workstation (CHI630E) at a scan rate of 0.1 mV s^{-1} between 0.01 and 3.0 V. AC voltage amplitude of 10 mV was employed to measure electrochemical impedance spectroscopy by the Autolab electrochemical workstation (PGSTAT302N) within the frequency ranging from 10 mHz to 100 KHz.

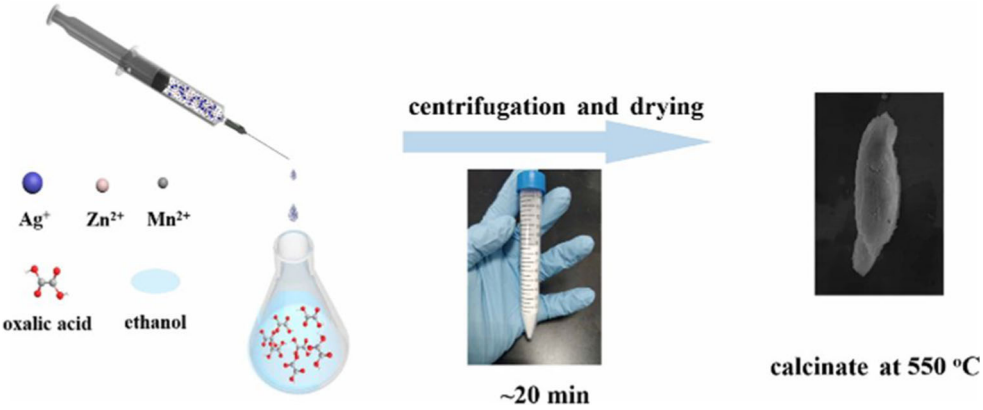

Fig. 1 The schematic illustration of the preparation process of Ag/ZMO composites

Results and discussion

Figure 1 briefly describes the preparation process of Ag/ZMO hybrids. Precipitate containing uniform distributed MnC_2O_4, ZnC_2O_4, and $Ag_2C_2O_4$ can be obtained by simply injecting aqueous solution A containing Ag^+, Zn^{2+}, and Mn^{2+} into a saturated oxalic acid ethanol solution. After being calcinated at 550 °C, mesoporous structured Ag/ZMO hybrids can be obtained due to the generation of massive CO_2 and H_2O gases.

Figure 2 shows the field-emission scanning electron microscopy (FESEM) images and elemental distribution of the ZMO, ZMO–Ag–1, ZMO–Ag–2, and ZMO–Ag–3, respectively. Figure 2a–h show the morphology of the ZMO, ZMO–Ag–1, ZMO–Ag–2, and ZMO–Ag–3 at different magnifications, which indicate that with the increase of Ag content, no morphology change has been observed. As can be seen from Fig. 2i–l, Zn, Mn, O, and Ag are uniformly distributed in the Ag/ZMO hybrids. In addition, energy-dispersive X-ray spectroscopy (EDS) analysis for all samples is conducted and the results are shown in Fig. S1. The EDS results demonstrate that the approximate weight ratio of Ag in the ZMO–Ag–1, ZMO–Ag–2, and ZMO–Ag–3 are 8.10%, 11.59%, and 21.04%, respectively, which is probably due to the difference of the solubility product constant of MnC_2O_4,

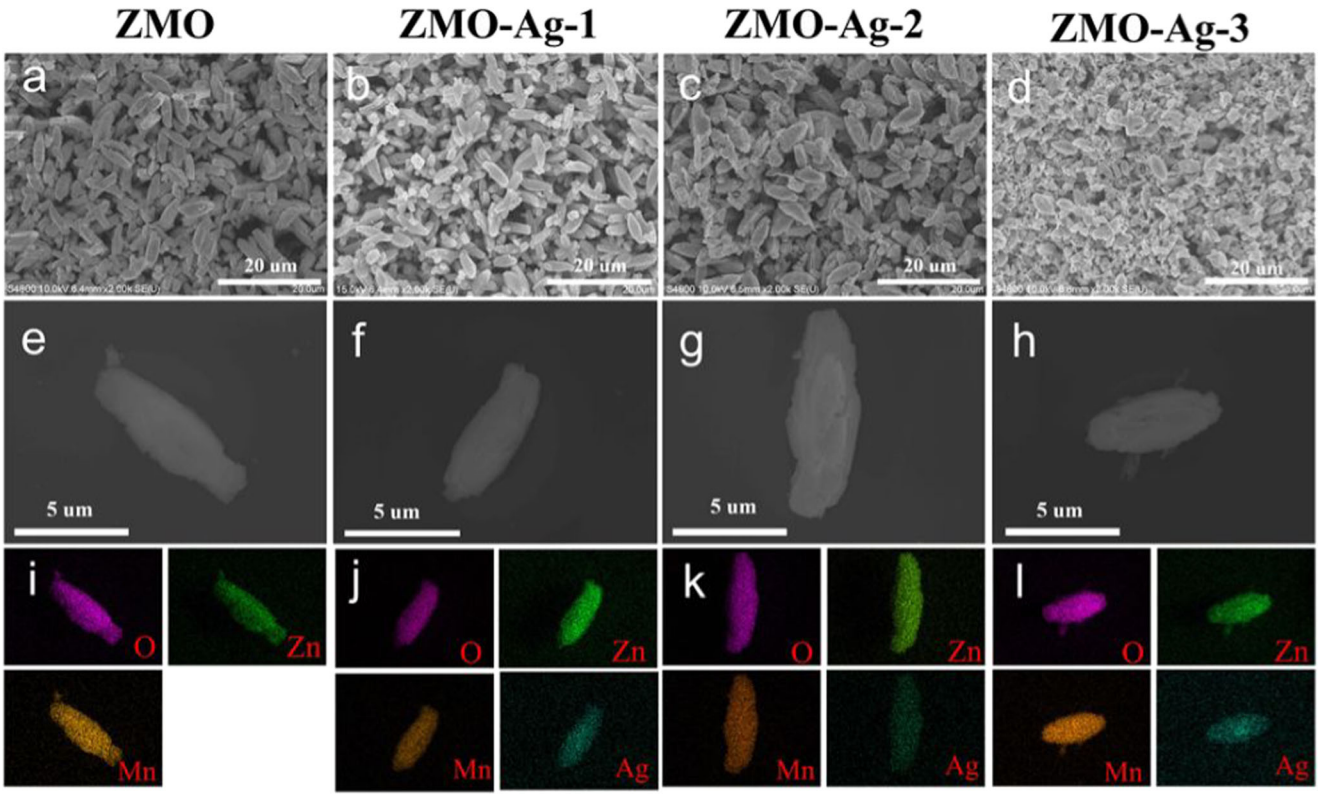

Fig. 2 SEM images of the as-prepared ZMO (**a**, **e**), ZMO–Ag–1 (**b**, **f**), ZMO–Ag–2 (**c**, **g**), and ZMO–Ag–3 (**d**, **h**). Element mapping of the as-prepared ZMO (**i**), ZMO–Ag–1 (**j**), ZMO–Ag–2 (**k**), and ZMO–Ag–3 (**l**)

ZnC_2O_4, and $Ag_2C_2O_4$. During the reaction process, the concentration of oxalic acid will gradually decrease, resulting in incomplete precipitation of Zn^{2+} and Mn^{2+} in the limited reaction time. Therefore, the designed weight ratios of Ag:ZMO are 1%, 3%, and 5%, but the actual weight ratio are 8.10%, 11.59%, and 21.04%, respectively.

The microstructure and morphology of ZMO–Ag–2 were further explored by high-resolution transmission electron microscopy (HRTEM). Combine the dark-field scanning transmission electron microscopy (DF-STEM) image (Fig. 3a) and elemental mapping images (Fig. 3d), Ag nanoparticles can be clearly observed and they are decorated on the ZMO matrix. Lattice fringes with *d* spacings of 0.232 and 0.303 nm are observed (Fig. 3c), which are in accordance with the (111) and (112) crystal planes of cubic Ag and spinel $ZnMn_2O_4$, respectively.

X-ray diffraction (XRD) patterns of the as-prepared materials and purchased Ag powder are shown in Fig. 4a. The characteristic peaks at 38.1°, 44.3°, and 64.4° can be accurately indexed to the (111), (200), and (220) planes of Ag (black line, JCPDS card No. 24–0783), respectively. While the peaks at 18.2°, 29.3°, 31.2°, 33.0°, 36.4°, 38.9°, 44.8°, 50.7°, 51.9°, 54.4°, 56.7°, 59.0°, 60.8°, and 65.2° are ascribed to the (101), (112), (200), (103), (211), (004), (220), (204), (105), (312), (303), (321), (224), and (400) planes of ZMO (red line, JCPDS card No. 24–1133), respectively. The diffraction peaks of the as-prepared materials can be well matched with ZMO and Ag, and no obvious shift of the diffraction peaks are observed with the increase of the weight ratio of Ag. Such results indicate that the obtained materials are the hybrid of bimetallic oxide ZMO and pure Ag. To further characterize the bonding information, normal Raman measurement is conducted on these samples with a 638-nm laser. As the Raman spectra shows in Fig. 4b, 324 cm^{-1}, 383 cm^{-1}, and 681 cm^{-1} are the main characteristic peaks of all samples. The peak at 681 cm^{-1} is assigned to the A_{1g} symmetry, 324 cm^{-1} and 383 cm^{-1} are characteristic peaks of the octahedral BO_6 site [14, 32, 39–41]. Comparing the Raman spectra of these three samples, the characteristic peaks of ZMO are gradually broadened as the increase of Ag ratio, which indicates that the crystallization of ZMO can be weakened with the addition of Ag. In addition, no characteristic peaks attributed to Ag_2O_2 and Ag_2O [42, 43] are detected, which further proves that silver is in the form of pure Ag metal rather metal oxides in the hybrids.

X-ray photoelectron spectroscopy (XPS) was conducted to further analyze the composition and elemental chemical states of Zn, Mn, and Ag in the as-prepared ZMO–Ag–2 hybrid. Figure 4c shows the survey XPS spectrum of the ZMO–Ag–2 hybrid which is mainly composed of Zn, Mn, Ag, and O elements. The peaks at 49.4 eV, 641.9 eV, 653.9 eV, 88.7 eV,

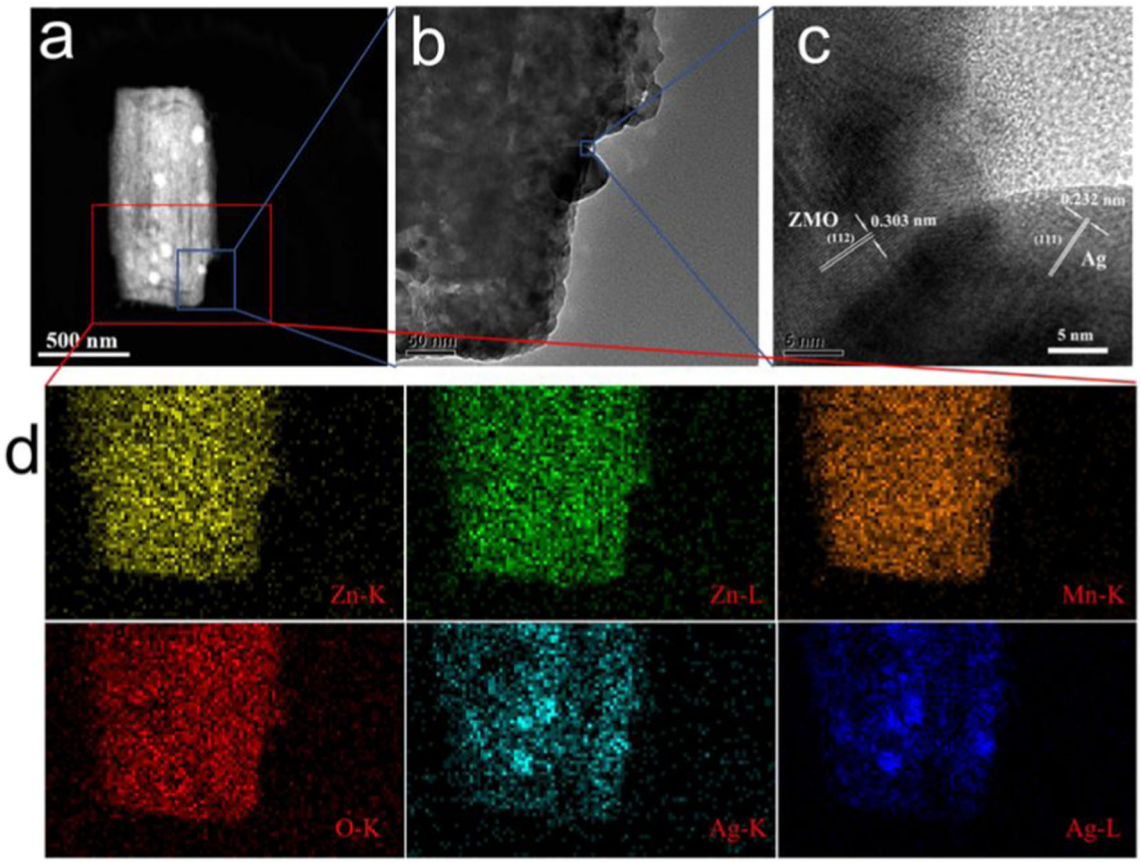

Fig. 3 Dark-field STEM image (**a**), HRTEM images (**b**, **c**), and elemental mapping (**d**) of ZMO–Ag–2

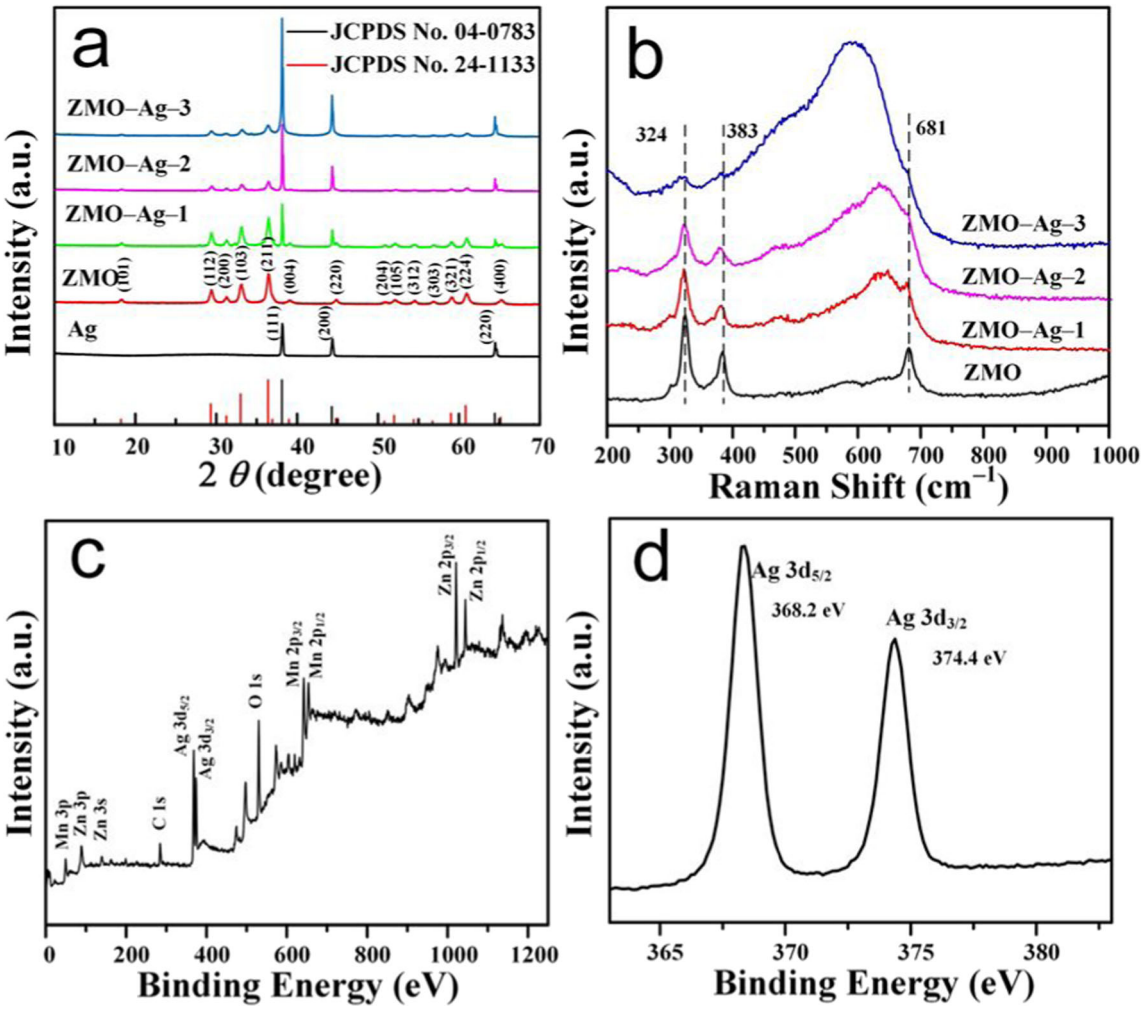

Fig. 4 XRD patterns (**a**) of purchased Ag powder, as-prepared ZMO, ZMO–Ag–1 ZMO–Ag–2, and ZMO–Ag–3. Raman spectra (**b**) of as-prepared ZMO, ZMO–Ag–1 ZMO–Ag–2, and ZMO–Ag–3. XPS spectra of (**c**) full scan, (**d**) Ag 3d of the as-prepared ZMO–Ag–2

139.8 eV, 1021.4 eV, and 1044.3 eV correspond to Mn 3p, Mn $2p_{3/2}$ Mn $2p_{1/2}$, Zn 3p, Zn 3 s, Zn $2p_{3/2}$, and Zn $2p_{1/2}$, respectively [14, 35, 44, 45]. As shown in Fig. S2a and S2b, the spin energy separation between Mn $2p_{3/2}$ and Mn $2p_{1/2}$ is 12 eV, while energy separation between the Zn $2p_{3/2}$ and Zn $2p_{1/2}$ is 22.9 eV, which indicates that the oxidation states of Mn and Zn are trivalent and bivalent, respectively [46]. The two peaks at binding energy of 368.2 eV and 374.4 eV corresponded to Ag $3d_{5/2}$ and Ag $3d_{3/2}$, respectively. The spin energy separation between Ag $3d_{5/2}$ and Ag $3d_{3/2}$ indicates that the valence of Ag is zero [47].

In order to investigate the performance of the Ag/ZMO hybrids as anode materials in lithium-ion batteries, the electrochemical performances of the ZMO, ZMO–Ag–1, ZMO–Ag–2, and ZMO–Ag–3 were measured. Figure 5a and c are the first three representative cyclic voltammogram (CV) curves of ZMO and ZMO–Ag–2 at a scan rate of 0.1 mV s^{-1} in the voltage range of 0.01–3.0 V (vs. Li/Li^+). During the first cathodic scan of ZMO, the first reduction peak appears at around 1.25 V, corresponding to the process of Mn^{3+} being reduced to Mn^{2+} [11]. Then, a wide reduction peak appears at 0.8 V, which is due to the formation of SEI film during the first discharge process [44]. The strongest reduction peak is around 0.3 V, which corresponds to the process of Mn^{2+} and Zn^{2+} being reduced to Mn^0 and Zn^0 and the forming process of $ZnLi_x$ alloy, respectively. During the anodic scan process, two obvious broaden oxidation peaks fall in 1.25 V and 1.55 V, which correspond to the fact that Mn^0 and Zn^0 are oxidated to Mn^{2+} and Zn^{2+}, respectively. In the two subsequent cycles, the main reduction peak shifts to 0.5 V, and the peak position of the oxidation peak does not change significantly [48, 49]. Compared with the CV curves of ZMO, a pair of redox peaks can be found at 0.1 V and 0.37 V in the CV of ZMO–Ag–2 (Fig. 5c), which are corresponding to the alloying and de-alloying process of Ag and Li. In order to verify this conclusion, purchased pure Ag powder was used to fabricate electrode and it was assembled in CR2032–coin batteries to evaluate its electrochemical performances. As shown in Fig. S3a, a pair of redox peaks at 0.1 and 0.37 V are observed which is consistent with that of ZMO–

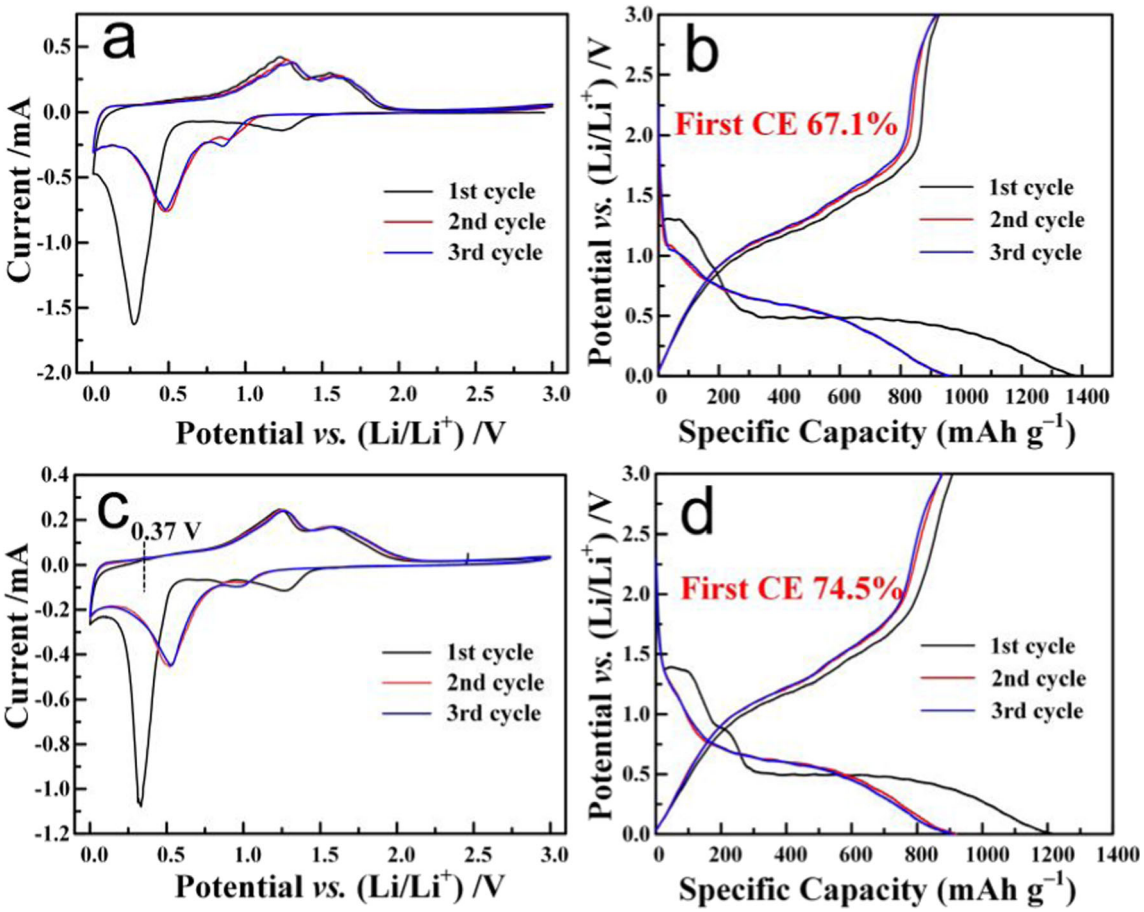

Fig. 5 CV curves of ZMO (**a**) and ZMO–Ag–2 (**c**) at a scan rate of 0.1 mV s^{-1}. Charge/discharge profiles of ZMO (**b**) and ZMO–Ag–2 (**d**) at the current density of 100 mA g^{-1}

Ag–2. Also, the first three charge/discharge curves of Ag are measured at current density of 100 mA g^{-1} (Fig. S3b). The discharge platform is around 0.1 V, and two charging platforms are located at 0.15 V and 0.37 V, respectively, which may be attributed to the progressive de-alloying process of $AgLi_x$ alloy [50–52]. The CV and charge/discharge characteristics of ZMO–Ag–1 and ZMO–Ag–3 (Fig. S4 and S5) are similar to that of ZMO–Ag–2.

Comparing the first three charge/discharge curves of the as-prepared materials and purchased Ag powder (Fig. 5b, d, S4b, S5b and S3b), the initial CE of ZMO, ZMO–Ag–1, ZMO–Ag–2, ZMO–Ag–3, and Ag are 67.1%, 73.2%, 74.5%, 79.2%, and 67.7%, respectively. It is clearly observed that the first cycle CE of Ag/ZMO hybrids increases along with the increase of Ag content. This indicates that the existence of Ag may have synergistic effect with ZMO and inhibits the continuous generation of SEI film in the first discharge process.

The electrochemical impedance spectroscopy (EIS) measurements were conducted to evaluate the electron conductivities of ZMO and Ag/ZMO hybrids. In Fig. 6a, the semicircle at high frequency decreases along with the increase of Ag content, which indicates that the charge transfer resistance of the battery is reduced with the addition of Ag particles. After 30 cycles at current density of 500 mA g^{-1}, the EIS spectrum of these electrodes was shown in Fig. S6. The cycled cell exhibits a much lower charge transfer resistance at high frequency compared with the uncycled cell, which is probably attributed to the activation of electrode materials.

The rate capacity displayed in Fig. 6b indicates that the ZMO–Ag–2 exhibits the best electrochemical performance. At 50, 200, 500, 1000, and 2000 mA g^{-1}, the ZMO–Ag–2 exhibits average capacity of 980, 810, 760, 740, and 700 mAh g^{-1}, respectively, whereas the ZMO exhibits average capacity of 970, 780, 680, 600, and 520 mAh g^{-1}. Therefore, it can be visualized that the addition of Ag particles can effectively improve the rate capacity of ZMO. Compared with ZMO, ZMO–Ag–1, and ZMO–Ag–2, both Ag and ZMO–Ag–3 have better cycle performance at high current density. With the increase of current density, only slight decreases of the capacities of Ag and ZMO–Ag–3 can be observed. Figure 6c displays the cycling performance of Ag, ZMO, ZMO–Ag–1, ZMO–Ag–2, and ZMO–Ag–3 at the current density of 100 mA g^{-1}. As shown in Fig. 6c, in the first 40 cycles, the capacity of ZMO is a little higher than that of ZMO–Ag–2. However, with the further increase of cycle

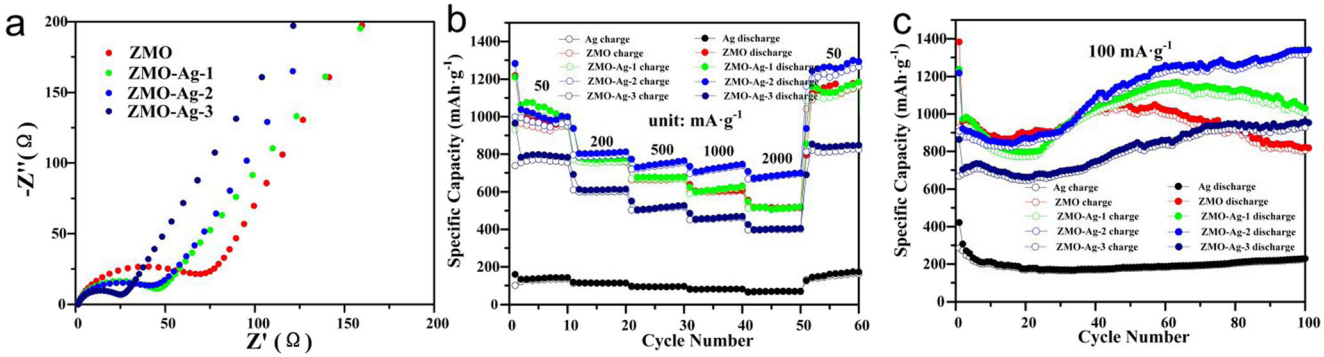

Fig. 6 Electrochemical impedance spectroscopy of the as-prepared materials (**a**). Rate performance (**b**), and cycle performance (**c**) of purchased Ag powders and as-prepared materials

number, the capacity of ZMO–Ag–2 gradually increases, while the capacity of ZMO decreases rapidly. The rapid decrease of the capacity of ZMO is probably due to the continuous growth of SEI film and gradual consumption of electrolyte during the charge and discharge processes. On the other hand, the decoration of Ag may lead to the formation of a thinner SEI film and may have a certain synergistic effect with ZMO during the lithiation/de-lithiation processes. After 100 cycles, an ultra-high capacity of about 1300 mAh g^{-1} can be obtained for the ZMO–Ag–2 hybrid. This cycle performance is better than most of the similar materials, as shown in Table S1. The cycling performance of different electrode materials are measured at 1000 mA g^{-1} and the results are shown in Fig. S7. Before applying 1000 mA g^{-1}, a small current density of 50 mA g^{-1} was applied to activate the electrode materials in the first three cycles. Compared with the other electrode materials, ZMO–Ag–2 exhibits the best cycle performance. After 150 cycles, ZMO–Ag–2 still has a capacity of 560 mAh g^{-1}, while the capacity of ZMO, ZMO–Ag–1, and ZMO–Ag–3 decreases to 440 mAh g^{-1}, 356 mAh g^{-1}, and 378 mAh g^{-1}, respectively. Although the cycle performances of ZMO–Ag–3 and Ag are ultra-stable, the capacities of ZMO–Ag–3 and Ag are much lower than that of ZMO–Ag–2, which is mainly attributed to the decrease of theoretical specific capacity of the composite with the increase of Ag content. The above lithium ion storage performances of the four as-prepared materials demonstrate that the addition of Ag can effectively improve the electrochemical performances of ZMO, and ZMO–Ag–2 shows the best properties than other Ag/ZMO composites.

To further prove that Ag nanoparticles can enhance the initial CE and cycling stability of ZMO, post-mortem analysis was conducted. The morphology analysis results of the cycled materials were shown in Fig. S8. It is obvious that the particle size of ZMO is greatly increased after 30 cycles, while no obvious increase of particle size in cycled Ag/ZMO hybrids are observed. Furthermore, there are a lot of creaked particles on the electrode surface of ZMO. On the contrary, cycled Ag/ZMO hybrids basically maintain the same shape as before the cycle. This may be one of the main reasons that Ag/ZMO hybrids show higher cycle stability than that of ZMO. Further in situ spectral and structural investigation is under progress to study the improvement mechanism by Ag addition.

Conclusions

In summary, Ag/ZMO hybrids with excellent cycle performance were designed and synthesized by a facile and scalable coprecipitation method, which was considered a promising method for industrial application. The electrochemical performance of different electrode materials showed that the addition of Ag can significantly improve the cycle stability of ZMO. After 100 cycles, the ZMO–Ag–2 could still maintain ultra-high capacity of 1300 mAh g^{-1} at 100 mA g^{-1}. The addition of Ag can effectively improve the conductivity of ZMO. Moreover, the existence of Ag may lead to the growth of a thinner SEI film on the surface of the electrode material which could greatly improve initial CE during charge/discharge process. Post-mortem analysis indicates the decoration of Ag nanoparticles may have a certain synergistic effect with ZMO during the lithiation/de-lithiation process and then result in a higher cycle stability. It is anticipated that our work may open up a new avenue to rapidly and massively produce various anode materials decorated with Ag nanoparticles for lithium-ion batteries.

Funding information This work was supported by the NSFC (21775127, 21503175 and 21521004), Fundamental Research Funds for the Central Universities (20720180016), General Financial Grant from the China Postdoctoral Science Foundation (2017 M622064), 2017 Xiamen Science and Technology Bureau Project (3502Z20173017), and Natural Science Foundation of Guangdong Province (2016A030308012).

Compliance with ethical standards

Conflict of interest The authors declare that they have no conflicts of interest.

References

1. Chu S, Majumdar A (2012) Opportunities and challenges for a sustainable energy future. Nature 488(7411):294–303. https://doi.org/10.1038/nature11475
2. Larcher D, Tarascon JM (2015) Towards greener and more sustainable batteries for electrical energy storage. Nat Chem 7(1):19–29. https://doi.org/10.1038/nchem.2085
3. Poizot P, Dolhem F (2011) Clean energy new deal for a sustainable world: from non-CO_2 generating energy sources to greener electrochemical storage devices. Energy Environ Sci 4(6):2003). https://doi.org/10.1039/c0ee00731e
4. Fukuda K, Kikuya K, Isono K, Yoshio M (1997) Foliated natural graphite as the anode material for rechargeable lithium-ion cells. J Power Sources 69(1–2):165–168. https://doi.org/10.1016/S0378-7753(97)02568-8
5. Yoshio M, Wang H, Fukuda K (2003) Spherical carbon-coated natural graphite as a lithium-ion battery-anode material. Angew Chem 115(35):4335–4338. https://doi.org/10.1002/ange.200351203
6. Bonino F, Brutti S, Reale P, Scrosati B, Gherghel L, Wu J, Müllen K (2005) A disordered carbon as a novel anode material in lithium-ion cells. Adv Mater 17(6):743–746. https://doi.org/10.1002/adma.200401006
7. Ji L, Rao M, Zheng H, Zhang L, Li Y, Duan W, Guo J, Cairns EJ, Zhang Y (2011) Graphene oxide as a sulfur immobilizer in high performance lithium/sulfur cells. J Am Chem Soc 133(46):18522–18525. https://doi.org/10.1021/ja206955k
8. Yi R, Dai F, Gordin ML, Chen S, Wang D (2013) Micro-sized Si-C composite with interconnected nanoscale building blocks as high-performance anodes for practical application in lithium-ion batteries. Adv Energy Mater 3(3):295–300. https://doi.org/10.1002/aenm.201200857
9. Tian G, Zhao Z, Sarapulova A, Das C, Zhu L, Liu S, Missiul A, Welter E, Maibach J, Dsoke S (2019) Understanding the Li-ion storage mechanism in a carbon composited zinc sulfide electrode. J Mater Chem A 7:15640–15653. https://doi.org/10.1039/c9ta01382b
10. Kacica CT, Wang LS, Chadha TS, Biswas P (2018) Oriented, one-dimensional tin dioxide-titanium dioxide composites as anode materials for lithium-ion batteries. Energy Technol 6(10):1966–1974. https://doi.org/10.1002/ente.201800103
11. Zhou L, Wu HB, Zhu T, Lou XW (2012) Facile preparation of $ZnMn_2O_4$ hollow microspheres as high-capacity anodes for lithium-ion batteries. J Mater Chem 22(3):827–829. https://doi.org/10.1039/c1jm15054e
12. Hu H, Guan B, Xia B, Lou XW (2015) Designed formation of $Co_3O_4/NiCo_2O_4$ double-shelled nanocages with enhanced pseudocapacitive and electrocatalytic properties. J Am Chem Soc 137(16):5590–5595. https://doi.org/10.1021/jacs.5b02465
13. Zhang G, Yu L, Wu HB, Hoster HE, Lou XW (2012) Formation of $ZnMn_2O_4$ ball-in-ball hollow microspheres as a high-performance anode for lithium-ion batteries. Adv Mater 24(34):4609–4613. https://doi.org/10.1002/adma.201201779
14. Kim JG, Lee SH, Kim Y, Kim WB (2013) Fabrication of free-standing $ZnMn_2O_4$ mesoscale tubular arrays for lithium-ion anodes with highly reversible lithium storage properties. ACS Appl Mater Inter 5(21):11321–11328. https://doi.org/10.1021/am403546s
15. Jiu H, Ren N, Jiang L, Zhang Q, Gao Y, Meng Y, Zhang L (2018) Hierarchical porous $CoMn_2O_4$ microspheres with sub-nanoparticles as advanced anode for high-performance lithium-ion batteries. J Solid State Electrochem 22(9):2747–2755. https://doi.org/10.1007/s10008-018-3987-y
16. Reddy AE, Anitha T, Muralee Gopi CVV, Durga IK, Kim H-J (2018) Facile synthesis of hierarchical $ZnMn_2O_4$@$ZnFe_2O_4$ microspheres on nickel foam for high-performance supercapacitor applications. New J Chem 42(4):2964–2969. https://doi.org/10.1039/c7nj04269h
17. Zhao Z, Tian G, Sarapulova A, Trouillet V, Fu Q, Geckle U, Ehrenberg H, Dsoke S (2018) Elucidating the energy storage mechanism of $ZnMn_2O_4$ as promising anode for Li-ion batteries. J Mater Chem A 6(40):19381–19392. https://doi.org/10.1039/c8ta06294c
18. Youn DH, Choi YH, Kim J-H, Han S, Heller A, Mullins CB (2018) Simple microwave-assisted synthesis of Delafossite $CuFeO_2$ as an anode material for sodium-ion batteries. ChemElectroChem 5:2419–2423. https://doi.org/10.1002/celc.201800548
19. Yao W, Zhao M, Dai Y, Tang J, Xu J (2017) Micro−/mesoporous zinc-manganese oxide/graphene hybrids with high specific surface area: a high-capacity, superior-rate, and ultralong-life anode for lithium storage. ChemElectroChem 4(1):230–235. https://doi.org/10.1002/celc.201600564
20. Cabo-Fernandez L, Mueller F, Passerini S, Hardwick LJ (2016) In situ Raman spectroscopy of carbon-coated $ZnFe_2O_4$ anode material in Li-ion batteries - investigation of SEI growth. Chem Commun 52(20):3970–3973. https://doi.org/10.1039/c5cc09350c
21. Bai J, Li X, Liu G, Qian Y, Xiong S (2014) Unusual formation of $ZnCo_2O_4$ 3D hierarchical twin microspheres as a high-rate and ultralong-life lithium-ion battery anode material. Adv Funct Mater 24(20):3012–3020. https://doi.org/10.1002/adfm.201303442
22. Xing Z, Ju Z, Yang J, Xu H, Qian Y (2012) One-step hydrothermal synthesis of $ZnFe_2O_4$ nano-octahedrons as a high capacity anode material for Li-ion batteries. Nano Res 5(7):477–485. https://doi.org/10.1007/s12274-012-0233-2
23. Bresser D, Paillard E, Kloepsch R, Krueger S, Fiedler M, Schmitz R, Baither D, Winter M, Passerini S (2013) Carbon coated $ZnFe_2O_4$ nanoparticles for advanced lithium-ion anodes. Adv Energy Mater 3(4):513–523. https://doi.org/10.1002/aenm.201200735
24. Gao Q, Yuan Z, Dong L, Wang G, Yu X (2018) Reduced graphene oxide wrapped $ZnMn_2O_4$/carbon nanofibers for long-life lithium-ion batteries. Electrochim Acta 270:417–425. https://doi.org/10.1016/j.electacta.2018.03.107
25. Zhang T, Yue H, Qiu H, Wei Y, Wang C, Chen G, Zhang D (2017) Nano-particle assembled porous core-shell $ZnMn_2O_4$ microspheres with superb performance for lithium batteries. Nanotechnology 28(10):105403. https://doi.org/10.1088/1361-6528/aa5a49
26. Zhong X-B, Wang H-Y, Yang Z-Z, Jin B, Jiang Q-C (2015) Facile synthesis of mesoporous $ZnCo_2O_4$ coated with polypyrrole as an anode material for lithium-ion batteries. J Power Sources 296:298–304. https://doi.org/10.1016/j.jpowsour.2015.07.047
27. Teh PF, Sharma Y, Ko YW, Pramana SS, Srinivasan M (2013) Tuning the morphology of $ZnMn_2O_4$ lithium ion battery anodes by electrospinning and its effect on electrochemical performance. RSC Adv 3:2812–2821. https://doi.org/10.1039/c2ra22943a
28. Zhang T, Yue H, Qiu H, Zhu K, Zhang L, Wei Y, Du F, Chen G, Zhang D (2015) Synthesis of graphene-wrapped $ZnMn_2O_4$ hollow microspheres as high performance anode materials for lithium ion batteries. RSC Adv 5(120):99107–99114. https://doi.org/10.1039/c5ra16667e
29. Huang T, Zhao C, Qiu Z, Luo J, Hu Z (2017) Hierarchical porous $ZnMn_2O_4$ synthesized by the sucrose-assisted combustion method for high-rate supercapacitors. Ionics 23(1):139–146. https://doi.org/10.1007/s11581-016-1817-8
30. Ren N, Jiu H, Jiang L, Zhang Q, Yu S, Gao Y, Gao Z, Zhang L (2018) Facile synthesis of hierarchical porous $ZnMn_2O_4$ rugby-balls on Ni foam for lithium-ion batteries with enhanced electrochemical properties. J Alloy Compd 740:28–35. https://doi.org/10.1016/j.jallcom.2017.12.362
31. Luo X, Zhang X, Chen L, Li L, Zhu G, Chen G, Yan D, Xu H, Yu A (2018) Mesoporous $ZnMn_2O_4$ microtubules derived from a bio-morphic strategy for high-performance lithium/sodium ion

batteries. ACS Appl Mater Inter 10(39):33170–33178. https://doi.org/10.1021/acsami.8b10111
32. Zhong X, Wang X, Wang H, Yang Z, Jiang Y, Li J, Tian Z (2018) Ultrahigh-performance mesoporous $ZnMn_2O_4$ microspheres as anode materials for lithium-ion batteries and their in situ Raman investigation. Nano Res 11(7):3814–3823. https://doi.org/10.1007/s12274-017-1955-y
33. Zhang T, Qiu H, Zhang M, Fang Z, Zhao X, Wang L, Chen G, Wei Y, Yue H, Wang C, Zhang D (2017) A unique 2D-on-3D architecture developed from $ZnMn_2O_4$ and CMK-3 with excellent performance for lithium ion batteries. Carbon 123:717–725. https://doi.org/10.1016/j.carbon.2017.08.013
34. Xie Q, Li F, Guo H, Wang L, Chen Y, Yue G, Peng DL (2013) Template-free synthesis of amorphous double-shelled zinc-cobalt citrate hollow microspheres and their transformation to crystalline $ZnCo_2O_4$ microspheres. ACS Appl Mater Inter 5(12):5508–5517. https://doi.org/10.1021/am400696x
35. Li P, Liu J, Liu Y, Wang Y, Li Z, Wu W, Wang Y, Yin L, Xie H, Wu M, He X, Qiu J (2015) Three-dimensional $ZnMn_2O_4$/porous carbon framework from petroleum asphalt for high performance lithium-ion battery. Electrochim Acta 180:164–172. https://doi.org/10.1016/j.electacta.2015.08.095
36. Liu B, Zhang J, Wang X, Chen G, Chen D, Zhou C, Shen G (2012) Hierarchical three-dimensional $ZnCo_2O_4$ nanowire arrays/carbon cloth anodes for a novel class of high-performance flexible lithium-ion batteries. Nano Lett 12(6):3005–3011. https://doi.org/10.1021/nl300794f
37. Han F, Li WC, Lei C, He B, Oshida K, Lu AH (2014) Selective formation of carbon-coated, metastable amorphous $ZnSnO_3$ nanocubes containing mesopores for use as high-capacity lithium-ion battery. Small 10(13):2637–2644. https://doi.org/10.1002/smll.201400371
38. Jiang H, Zhang H, Fu Y, Guo S, Hu Y, Zhang L, Liu Y, Liu H, Li C (2016) Self-volatilization approach to mesoporous carbon nanotube/silver nanoparticle hybrids: the role of silver in boosting Li ion storage. ACS Nano 10(1):1648–1654. https://doi.org/10.1021/acsnano.5b07367
39. Zhou W, Wang D, Zhao L, Ding C, Jia X, Du Y, Wen G, Wang H (2017) Template-free fabrication of graphene-wrapped mesoporous $ZnMn_2O_4$ nanorings as anode materials for lithium-ion batteries. Nanotechnology 28(24):245401. https://doi.org/10.1088/1361-6528/aa6ec4
40. Sun Q, Bijelić M, Djurišić AB, Suchomski C, Liu X, Xie M, Ng AMC, Kong Li H, Shih K, Burazer S, Skoko Ž, Djerdj I, Popović J (2017) Graphene-oxide-wrapped $ZnMn_2O_4$ as a high performance lithium-ion battery anode. Nanotechnology 28(45):455401. https://doi.org/10.1088/1361-6528/aa8a5b
41. Bijelić M, Liu X, Sun Q, Djurišić AB, Xie MH, Ng AMC, Suchomski C, Djerdj I, Skoko Ž, Popović J (2015) Long cycle life of $CoMn_2O_4$ lithium ion battery anodes with high crystallinity. J Mater Chem A 3(28):14759–14767. https://doi.org/10.1039/c5ta03570h
42. Waterhouse GIN, Bowmaker GA, Metson JB (2001) The thermal decomposition of silver (I, III) oxide: a combined XRD, FT-IR and Raman spectroscopic study. Phys Chem Chem Phys 3(17):3838–3845. https://doi.org/10.1039/b103226g
43. Wang H, Li J, Zhou M, Guan Q, Lu Z, Huo P, Yan Y (2015) Preparation and characterization of Ag_2O/SWNTs photocatalysts and its photodegradation on tetracycline. J Ind Eng Chem 30:64–70. https://doi.org/10.1016/j.jiec.2015.05.002
44. Fan B, Hu A, Chen X, Zhang S, Tang Q, Wang J, Deng W, Liu Z, Xiao K (2016) Hierarchical porous $ZnMn_2O_4$ microspheres as a high-performance anode for lithium-ion batteries. Electrochim Acta 213:37–45. https://doi.org/10.1016/j.electacta.2016.07.030
45. Zeng X, Shi L, Li L, Yang J, Cheng X, Gao M (2015) The preparation of flowerlike $ZnMn_2O_4$ microspheres assembled with porous nanosheets and their lithium battery performance as anode materials. RSC Adv 5(86):70379–70386. https://doi.org/10.1039/c5ra11473j
46. Zhong M, Yang D, Xie C, Zhang Z, Zhou Z, Bu XH (2016) Yolk-Shell MnO@$ZnMn_2O_4$/N-C Nanorods derived from alpha-MnO_2/ZIF-8 as anode materials for lithium ion batteries. Small 12(40):5564–5571. https://doi.org/10.1002/smll.201601959
47. Han SW, Kim Y, Kim K (1998) Dodecanethiol-derivatized Au/Ag bimetallic nanoparticles: TEM, UV/VIS, XPS, and FTIR analysis. J Colloid Inter Sci 208(1):272–278. https://doi.org/10.1006/jcis.1998.5812
48. Yuan C, Zhang L, Hou L, Zhou L, Pang G, Lian L (2015) Scalable room-temperature synthesis of mesoporous nanocrystalline $ZnMn_2O_4$ with enhanced lithium storage properties for lithium-ion batteries. Chem Eur J 21(3):1262–1268. https://doi.org/10.1002/chem.201404624
49. Yao W, Xu J, Wang J, Luo J, Shi Q, Zhang Q (2015) Chemically integrated multiwalled carbon nanotubes/zinc manganate nanocrystals as ultralong-life anode materials for lithium-ion batteries. ACS Sustain Chem Eng 3(9):2170–2177. https://doi.org/10.1021/acssuschemeng.5b00434
50. Lin X-M, Diemant T, Mu X, Gao P, Behm RJ, Fichtner M (2018) Spectroscopic investigations on the origin of the improved performance of composites of nanoparticles/graphene sheets as anodes for lithium ion batteries. Carbon 127:47–56. https://doi.org/10.1016/j.carbon.2017.10.076
51. Wachtler M, Winter M, Besenhard JO (2002) Anodic materials for rechargeable Li-batteries. J Power Sources 105(2):151–160. https://doi.org/10.1016/S0378-7753(01)00934-X
52. Taillades G, Sarradin J (2004) Silver: high performance anode for thin film lithium ion batteries. J Power Sources 125(2):199–205. https://doi.org/10.1016/j.jpowsour.2003.07.004